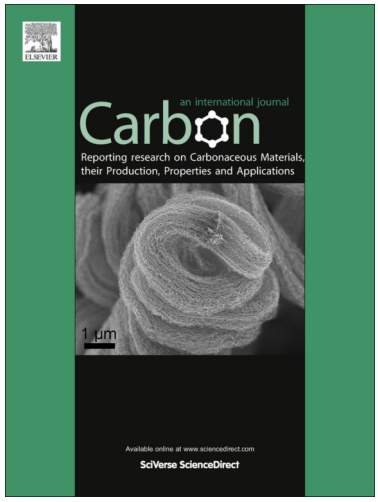

Methods to Assess the Impact of UV Irradiation on the Surface Chemistry and Structure of Multiwall Carbon Nanotube Epoxy Nanocomposites

Elijah J. Petersen, Thomas Lam, Justin M. Gorham, Keana C. Scott, Christian J. Long, Deborah Stanley, Renu Sharma, J. Alexander Liddle, Bastien Pellegrin, Tinh Nguyen

PII: S0008-6223(13)01158-5
DOI: http://dx.doi.org/10.1016/j.carbon.2013.12.016
Reference: CARBON 8597

To appear in: *Carbon*

Received Date: 27 September 2013
Accepted Date: 5 December 2013

Please cite this article as: Petersen, E.J., Lam, T., Gorham, J.M., Scott, K.C., Long, C.J., Stanley, D., Sharma, R., Alexander Liddle, J., Pellegrin, B., Nguyen, T., Methods to Assess the Impact of UV Irradiation on the Surface Chemistry and Structure of Multiwall Carbon Nanotube Epoxy Nanocomposites, *Carbon* (2013), doi: http://dx.doi.org/10.1016/j.carbon.2013.12.016

Methods to Assess the Impact of UV Irradiation on the Surface Chemistry and Structure of Multiwall Carbon Nanotube Epoxy Nanocomposites

Elijah J. Petersen[1*], *Thomas Lam*[2], *Justin M. Gorham*[3], *Keana C. Scott*[3], *Christian J. Long*[2,4], *Deborah Stanley*[5], *Renu Sharma*[2], *J. Alexander Liddle*[2], *Bastien Pellegrin*[6], *Tinh Nguyen*[5*]

[1]Biosystems and Biomaterials Division, NIST, Gaithersburg, MD 20899, United States

[2]Center for Nanoscale Science and Technology, NIST, Gaithersburg, MD 20899, United States

[3]Materials Measurement Science Division, NIST, Gaithersburg, MD 20899, United States

[4]Maryland Nanocenter, University of Maryland, College Park, MD 20742, United States

[5]Engineering Laboratory, NIST, Gaithersburg, MD 20899, United States

[6]LGC, Université de Toulouse, 31062 Toulouse, France.

* Corresponding authors. Tel: 301-975-6718. E-mail address tinh.nguyen@nist.gov (T. Nguyen) and 301-975-8142, elijah.petersen@nist.gov (E. J. Petersen)

One of the most promising applications of nanomaterials is as nanofillers to enhance the properties of polymeric materials. However, the effect of nanofillers on polymers subjected to typical environmental stresses, such as ultraviolet (UV) radiation, high humidity, or elevated temperatures, is not well understood. This stems partly from a lack of a single analytical method to assess these impacts. In this study, multiwall carbon nanotube (MWCNT) epoxy nanocomposite materials were exposed to carefully controlled UV doses (equivalent of up to ≈ 4 years in Florida). A suite of microscopic, spectroscopic and gravimetric techniques were optimized and used to assess changes occurring in the sample mass, surface chemistry, and surface and sub-surface morphology after UV irradiation. Overall, photodegradation of the epoxy matrix was retarded by the presence of the 3.5% MWCNT filler, suggesting that MWCNTs may enhance the lifetime of nanocomposite materials. Multiple microscopic and spectroscopic techniques clearly showed accumulation of MWCNTs on the nanocomposite surface that grew with increasing UV dose, a finding that may be significant with regard to the potential risk of MWCNT release during the nanocomposite lifetime. These analytical methods will help enable a robust and informative assessment of transformations in polymer nanocomposites subject to environmental stresses.

1. Introduction

One prominent area of nanotechnology that is expected to dramatically increase in future years is use of nanocomposites in a variety of consumer, industrial, and manufacturing applications. Nanocomposite materials contain a nanofiller, which is defined as any particle with a characteristic dimension between 1 nm and 100 nm, incorporated into a matrix material (*e.g.*, polymer, ceramic, etc.) in order to enhance the useful properties of the original matrix material. For example, incorporating multiwall carbon nanotubes (MWCNTs) into polymer matrices (i.e., MWCNT polymer nanocomposites) yields materials whose properties can readily be engineered for applications in aerospace [1], construction [2], and consumer products [3]. MWCNT nanocomposites offer important novel or substantially improved properties (e.g., mechanical, electrical, and light weight) compared to traditional fiber-reinforced polymer composites [4, 5].

While incorporating nanofillers to form a polymer nanocomposite have received significant research interest, far fewer studies have assessed the impact of environmental stresses (e.g., biodegradation, ultraviolet (UV) light, and rain) on nanocomposites and on the potential release of nanomaterials [3, 6-10]. The release of carbon nanotubes (CNTs) from nanocomposites has been investigated during machining processes (e.g., sanding, solid core drilling, and cutting) [11-15] and in end use applications during which the nanocomposites may be exposed to abrasion, photo or hydrolytic degradation [14, 16-21]. CNT release is particularly important given their potential environmental and human health risks [6, 22-24]. In environmental uptake studies, CNT accumulation at high concentrations has been observed in water fleas (*Daphnia magna*) [25, 26] but not in soil or sediment organisms [6, 27-31]. CNTs have also shown the capacity to cause inflammation, oxidative stress, and potential genotoxicity that may cause risks for workers if exposure is not controlled [23, 32].

Studies on MWCNT release from polymer nanocomposites have sought to determine release rates and whether MWCNTs are released as free particles or are encapsulated in a polymer. While two studies have shown the release of free MWCNTs from an epoxy-based nanocomposite after abrasion [17] and sanding (but only for the 4 % MWCNT condition) [15], release of individual MWCNTs has generally not been detected [11-14, 16, 21]. These observations do not, however, preclude the possibility of MWCNT release under certain circumstances. In order to assess the likelihood of free MWCNT generation, it is necessary to understand the mechanisms that may lead to its occurrence. This information is needed for life cycle assessments of polymer nanocomposites. In this study, we focus on the effects of matrix degradation induced by UV radiation (i.e., photodegradation) – the most important degradation process for polymeric materials exposed to weathering environments [33]. While several studies have shown MWCNT surface accumulation after UV exposure [14, 16, 20, 21], the changes in the structure and surface chemistry of the nanocomposite were not fully assessed – principally due to a lack of optimized analytical methods – making the development of accurate mechanistic models, and thus prediction of release scenarios, challenging.

In this study, we have developed and applied a comprehensive suite of analytical methods to investigate dose-dependent effects of UV irradiation on the fate of MWCNTs and surface chemistry and structure of a MWCNT epoxy nanocomposite. Accelerated testing was performed using intense UV irradiation in the same spectral regime as the UV portion of natural sunlight (295 nm to 400 nm) at elevated temperature (50 °C) and humidity (75 % relative humidity). Surface and bulk material chemistry and structure were analyzed using gravimetry, scanning electron microscopy (SEM), atomic force microscopy (AFM), Fourier transform infrared spectroscopy in attenuated total reflection mode (FTIR-ATR), and X-ray photoelectron

spectroscopy (XPS). Additionally, the sub-surface structure of the nanocomposites was investigated using SEM, bright-field transmission electron microscopy (TEM), and energy-filtered TEM (EFTEM) after preparing cross-sections using cryo-fracturing or a focused ion beam (FIB). This allowed for an investigation of the mechanism of damage to polymer MWCNT nanocomposite as a function of increasing UV exposure. As we show, no single analytical method provided all the necessary information – it was essential to develop and optimize a range of techniques to provide a complete picture. While most prior studies focused almost exclusively on NP release, this is the first study to investigate in depth the transformations of both the surface chemistry and surface morphology of a MWCNT polymer nanocomposite during UV degradation processes using a suite of optimized analytical methods. Further, the results obtained are helpful in assessing potential risks during the life cycle of MWCNT polymer nanocomposites, and the methods developed will facilitate a robust assessment of the impact of environmental stresses on polymer nanocomposites in future studies.

2. Experimental Section

MWCNT epoxy nanocomposite samples were prepared by mixing a MWCNT-pre-dispersed liquid epoxy resin with an aliphatic amine curing agent, and the mixture was then drawn down on a Mylar sheet to produce free standing films. These samples were subjected to a series of precisely controlled UV doses up to 1089 MJ/m^2 using the National Institute of Standards and Technology (NIST) SPHERE (Simulated Photodegradation *via* High Energy Radiant Exposure) [34] in a 50 ^{o}C and 75 % relative humidity (RH) environment. Samples prepared identically but without MWCNTs were also fabricated and were similarly exposed. The UV-irradiated MWCNT epoxy nanocomposites were then analyzed with a suite of methods to investigate the bulk material, its surface chemistry, and the surface and sub-surface structure. The methods will

be described in the order of macroscopic analysis (gravimetry), followed by surface analysis techniques (FTIR-ATR, XPS, AFM, and SEM), and then assessments of the nanoscale features of cross-sections using EFTEM. Finally, scratch lithography using AFM was investigated as a novel technique to assess the potential release of MWCNTs from the surface and test the resistance of the surface to scratching at different normal loads.

2.1 *Materials*

The epoxy polymer was a stoichiometric mixture of a typical diglycidyl ether of bisphenol A epoxy resin (189 equivalent mass) (EPON 828, Resolution Performance Products) and an aliphatic polyetheramine curing agent (73.3 equivalent mass) (Jeffamine T403, Huntsman Corporation). MWCNTs were supplied commercially as a 5 % mass fraction (based on the mass of the epoxy resin) pre-dispersed in the same liquid epoxy resin (Zyvex). Besides the epoxy resin and the MWCNT concentration, other information about this nanofiller pre-dispersed epoxy product, including the MWCNT manufacturer, amount of residual catalyst, additive or surfactant, etc., is not available. To better understand the starting material, the sizes of the MWCNTs were investigated using SEM after extraction from the epoxy resin (see Supplemental Material). The average MWCNT diameter was 23.4 nm ± 5.8 nm (n=200; uncertainty represents one standard deviation), and the lengths predominately ranged between 200 nm and 2 μm; challenges associated with accurately obtaining a MWCNT length distribution have been previously described [35]. Micrographs and a histogram of the MWCNT diameters are provided in Figure S1.

Free-standing films of unfilled (neat) epoxy and epoxy nanocomposite containing approximately 3.5 % mass fraction of MWCNTs (based on mass of solid amine-cured epoxy) were prepared following the steps shown in Figure S2. Accordingly, amine curing agent was added to the neat

epoxy resin or thoroughly stirred 5 % MWCNT-containing epoxy resin, and the mixture was stirred for 1 h using a magnetic stirrer. (Note that after adding the amine curing agent, the 5 % mass fraction MWCNT in the neat epoxy resin becomes 3.5 % mass fraction MWCNT in the cured epoxy composite.) After the mixing step, the epoxy/amine and the epoxy/amine/MWCNT mixtures were degassed for 1 h at room temperature and drawn down on a Mylar sheet (a good release paper for epoxy-based products) to produce free standing films with a dry-film thickness between 125 μm and 150 μm. Unfilled and nanocomposite films were cured at ambient conditions (24 °C and 45 % relative humidity) for 4 d, followed by post-curing at 110 °C for 1 h in an air circulating oven. The 4 d ambient cure allowed a gradual increase in viscosity, which facilitated the escape of any residual trapped air that was introduced during mixing and film application. The quality of all composite films was good with no evidence of air bubbles or defects and the air surface was smooth (highly glossy), as shown in the AFM images given in the result section (e.g., Figure S6). All specimens were well cured, as evidenced by no further Fourier transform infrared spectroscopy (FTIR) intensity decrease of the epoxide band at 915 cm^{-1}. The glass transition temperature, Tg, of the cured film was 102 ± 2 ^{o}C (by dynamic mechanical analysis; uncertainty represents one standard deviation, n = 3). The chemical structures of the epoxy resin, the amine curing agent, and the crosslinked cured epoxy have been previously described [8].

2.2 *UV Irradiation*

Specimens of neat epoxy and nanocomposites having a dimension of 25 mm x 25 mm were exposed to 50 ^{o}C/75 % RH condition in a 2 m integrating sphere-based weathering chamber, referred to as the NIST SPHERE [34]. The elevated temperature was used to accelerate the chemical degradation, while the 75 % RH is a typical summer value. This

SPHERE UV device utilizes a mercury arc lamp system that produces a collimated and highly uniform UV flux of approximately 480 W/m^2 in the 295 nm to 400 nm wavelength. It can precisely control the relative humidity (RH) and temperature. A table showing the UV dose after exposure in the SPHERE for various durations is provided in Table S1. Dose, in MJ/m^2, is defined as the total energy of UV radiation impinging on the specimen surface at a particular time per unit irradiated area. The highest accelerated UV dose was equivalent to ≈ 4 years in Florida; the NIST SPHERE only supplies radiation from 295 nm to 400 nm and this comparison is for the estimated dosage in Florida (285 MJ/m^2 per year) for the wavelengths between 295 nm and 385 nm [36]. Because the visible and infrared radiation of the UV source had been removed, without external heating, the temperature in this UV chamber is about 27 ^{o}C ± 2 ^{o}C. Thus, an external heat source was used to increase the temperature to 50 ^{o}C to promote more rapid degradation. Specimens having the air surface facing the UV source, which were mounted on a special sample holder, were removed at specified accumulated doses (i.e., at specified time intervals) for characterization.

2.3 *Mass Loss Measurements*

Mass loss of both neat epoxy and nanocomposite as a function of exposure to UV radiation were measured. The mass loss was determined with an analytical balance (Mettler Toledo AB265-S, Columbus, OH) having a mass resolution of 10^{-5} g.

2.4 *Fourier transform infrared spectroscopy-attenuated total reflection (FTIR-ATR)*

Chemical degradation was assessed by FTIR-ATR using a ZnSe prism and at a 45° incident angle. For an ideal prism-sample interaction, the probing depth of the ATR technique is a function of incident angle, radiation wavelength, and refractive indices of the internal reflection element (i.e., prism) and the sample. For the ZnSe prism and 45^{o} incident angle used in this

study, the probing depth of ATR technique in the epoxy polymer (refractive index 1.5) in the infrared region of 800 cm^{-1} to 3600 cm^{-1} wavenumber, as calculated by the internal reflection penetration depth equation [37], is between 0.5 μm and 2.5 μm from the surface. All FTIR spectra were the average of 128 scans and recorded at a resolution of 4 cm^{-1} using a spectrometer equipped with a liquid nitrogen-cooled mercury cadmium telluride (MCT) detector (Nexus 670, Thermo Nicolet, Madison, Wisconsin). Dry air was used as the purge gas. The peak height was used to represent the infrared intensity, which is expressed in absorbance, A. All FTIR results were the average of three specimens.

2.5 *X-ray photoelectron spectroscopy (XPS)*

XPS was performed on a Kratos Axis Ultra DLD spectrophotometer (Chestnut Ridge, NY). Sample preparation involved loading all MWCNT epoxy nanocomposites onto a sample bar, with the samples being held down by metal fasteners. All spectra shown in this study were acquired using 150 W (10 mA, 15 kV), monochromatic, Al Kα X-rays with photoelectrons being collected by a hemispherical analyzer at 0 degrees from the surface normal at a pass energy of 20 eV. Data collection for each C (1s) region was taken at 0.030 eV steps with a dwell time of 800 ms/step for 2 sweeps. When activated, the charge neutralizer operated at 1.86 A and 3.64 V. Lastly, controls were run for both the MWCNTs and the pure epoxy, the latter of which could only be measured with the charge neutralizer due to its insulating properties. However, it is important to note that unless specified, XPS data presented was taken without the charge neutralizer. Spectral analysis was conducted using CasaXPS (CasaXPS LTD, Teignmouth, UK) and Shirley backgrounds were fitted to each C (1s) region. Chemical compositions were not determined in this study due to either charging or inability to separate the asymmetric MWCNT

peak from the epoxy components. All neat epoxy and MWCNT epoxy nanocomposite spectra are presented with no energy adjustment.

2.6 *Atomic Force Microscopy (AFM)*

AFM was performed using a Cypher AFM (Asylum Research/Oxford Instruments, Santa Barbara, CA) for all samples except for the highest UV dose sample (1089 MJ/m^2). Due to the large roughness of this sample, it was imaged using an MFP-3D AFM (Asylum Research/Oxford Instruments, Santa Barabara, CA) which has a larger scan range. All images were acquired in air at room temperature and in tapping mode using Si cantilevers with a spring constant of ≈ 40 N/m and a resonant frequency of ≈ 300 kHz. Image processing was performed using Gwyddion [38] in order to produce the 3D renderings of sample topography, as well as to remove minor streaks and steps in the topography, which are associated with AFM tip contamination.

2.7 *Scanning Electron microscopy (SEM)*

Surface and subsurface morphologies of the UV irradiated MWCNT epoxy nanocomposites were analyzed by SEM using a Zeiss Supra-55VP Field Emission SEM. Surface analysis was performed using a 5 kV acceleration voltage. Cross sections for subsurface analysis were prepared by freeze fracture. To visualize the MWCNT morphology within the embedded matrix by charge contrast imaging, the cross-sectional analysis was performed at 15kV acceleration voltage [39].

2.8 *Transmission Electron microscopy (TEM)*

Though freeze fracture cross sections are useful for SEM analysis, they are not a true planar section that would allow for nanoscale imaging of the subsurface. For a nanoscale resolution of planar cross sections, TEM samples were prepared using a FEI Helios NanoLab

650 Focused Ion Beam Scanning Electron Microscope (FIB SEM) equipped with a micromanipulator (Omniprobe Autoprobe 200.2 micromanipulator, Dallas, TX). The UV irradiated MWCNT epoxy nanocomposite samples were sputter coated with Au using a sputter coater (Cressington 208HR sputter coater, Watford, UK) to prevent charging and also to provide protection against the ion beam damage during the TEM sample preparation process. TEM thin sections were created using an *in situ* lift out method similar to that previously described [40]. Briefly, a thin layer (200 nm) of Pt was deposited using the electron beam at 2 kV and 6.4 nA and sample at 0 tilt. One 2-µm layer of Pt was deposited using the ion beam at 30 kV and 0.23 nA on the same location. Area surrounding the protective layer was removed using 9.3 nA and 2.5 nA ion beam and U shaped undercut was made using 0.23 nA ion beam. The remaining thick coupon was attached to the probe needle and reattached to a grid straddling a v-shaped groove on a TEM grid (Figure S3). Additional 1 µm of Pt was deposited on top of the coupon as well as the side walls of the coupon. Side wall Pt deposition was achieved by rotating the sample stage ± 90 degrees at 0 tilt. These Pt sidewalls provide the necessary stiffening of the thin polymer section. The coupon was thinned to 2 kV electron transparency using 30 kV ion beam and progressively lower beam currents ranging from 0.43 nA to 80 pA and then further cleaned using a 5 kV, 41 pA ion beam.

TEM using a FEI Titan™ 80-300 S/TEM equipped with an imaging filter (Gatan Model 963 Quantum, Pleasanton, CA) was used to collect bright-field and energy-filtered transmission electron microscopy (EFTEM) data. EFTEM images were collected at 300 kV using a slit of 5 eV centered at 18 eV and at 27 eV with 5 s exposures using a CCD (charge-coupled detector) with 2x binning. The 27 eV and 18 eV images were corrected for spatial drift [41] and a ratio of the 27 eV and 18 eV images were performed for contrast enhancement.

2.9 *Scratch Lithography*

In scratch lithography, lines are patterned on a sample surface by dragging an AFM tip across the surface while maintaining a constant normal load. In this study, a series of increasing normal loads were used to produce several such lines in order to assess the load-dependence of surface damage from the AFM tip. To establish the same regions of interest for AFM and post scratch analysis SEM, Pt markers (2 µm by 8 µm, 0.5 µm thick) were ion beam deposited using a Focused Ion Beam Scanning Electron Microscope (FIB SEM; FEI Helios NanoLab 650, Hillsboro, OR). Scratch lithography was performed using a Cypher AFM. A diamond coated AFM tip (model DCP11, from NT-MDT) was used in order to avoid artifacts associated with tip wear during scratching. The spring constant of the lever was 10.8 N/m ±1 N/m as measured using the thermal spectrum method [42]. According to the manufacturer, the diamond coating is ≈ 100 nm thick, and the radius of curvature is ≈ 100 nm. Scratching was performed in contact mode at a tip speed of 1 µm/s, and at a fixed normal load for each scratched line. A single pass was made at each scratched line. After scratching the sample, the tip was changed to a standard tapping mode tip and the scratched region was then imaged in tapping mode. Post scratch lithography SEM analysis was performed using a 5 kV acceleration voltage also using the FEI Helios NanoLab 650 Focused Ion Beam Scanning Electron Microscope (FIB SEM).

3. Results and Discussion

3.1 *Effects of UV Irradiation on Bulk Material*

The mass loss of neat epoxy and 3.5 % MWCNT epoxy nanocomposite samples as a function of UV dose in the NIST SPHERE is displayed in Figure 1. Except for a small increase in mass at very early exposure, the mass loss in both materials increased with increasing UV

dose. The early mass increase was probably due to moisture uptake when the samples were transferred from the 45 % RH ambient condition to the 75 % RH of the exposure chamber. At this early stage, the mass gained by the moisture uptake was greater than the mass loss caused by the nanocomposite degradation; thus, a net mass increase was observed. Figure 1 shows that both the amount and rate of mass loss for the MWCNT epoxy nanocomposite were lower than those for the neat epoxy. At a dosage of 1089 MJ/m^2, the mass loss of the neat epoxy was more than twice that of the MWCNT epoxy nanocomposite, approximately 2.3 % and 1 %, respectively. These results are consistent with a previous report for a 0.72 % MWCNT epoxy nanocomposite [20]. The lower rate of mass loss of the nanocomposite is attributed to the ability of MWCNTs to retard the degradation of the epoxy matrix (i.e., photostabilization), as will be later demonstrated by the FTIR results (see Figures 2 and 3).

3.2 *Effects of UV Irradiation on Nanocomposite Surface Chemistry*

FTIR-ATR was used to follow the chemical degradation of neat epoxy and 3.5 % MWCNT epoxy nanocomposites (see Figures 2 and S4). Any chemical changes observed for neat epoxy and MWCNT epoxy nanocomposite (assuming that the refractive index of the surface layer of the 3.5 % MWCNT epoxy nanocomposite is similar to that of the neat epoxy) are an average of the material layer within 2.5 μm from the surface. The chemical degradation by UV irradiation of polymers and their nanocomposites can be conveniently studied by following the intensity changes of various FTIR bands as a function of UV dose or exposure time. In this study, we utilized the FTIR difference spectroscopy technique, in which an increase or a decrease of a particular functional group can be easily discerned and quantified. Figure 2 displays difference spectra (spectra taken at various UV doses minus the spectrum of the sample before irradiation) as a function of UV dose for neat epoxy (Figure 2A) and 3.5 % MWCNT epoxy nanocomposite

(Figure 2B). As the UV dose increased, the intensity of various bands of the epoxy structure decreased, including the bands at 1508 cm^{-1} (benzene ring) and at 1245 cm^{-1} (C-O), while new bands appeared in the 1620 cm^{-1} to 1740 cm^{-1} region due to the formation of C=C and various carbonyl groups (C=O) such as aldehydes and ketones. These changes are due to photodegradation of amine-cured epoxy by UV radiation in the 295 nm to 400 nm wavelength, leading to extensive scission of the main chains of the epoxy [43-46]. Although amine-cured epoxy polymers are used extensively for a variety of exterior applications, the presence of UV absorbing aromatic rings and electron-donor nitrogen in the chemical structure makes this epoxy-based material susceptible to UV attack. Details of the photodegradation mechanisms of amine-cured epoxies are beyond the scope of the present study but can be found in the above references.

The strongest absorption band of the epoxy chemical structure at 1508 cm^{-1} and the newly-formed band at 1726 cm^{-1} (attributed to aldehyde C=O stretching) were employed to follow the degradation and oxidation, respectively, of neat epoxy and 3.5 % MWCNT epoxy nanocomposite samples as a function of UV dose. These results are depicted in Figure 3. Note that, although the highest exposed UV dose was 1089 MJ/m^2, the FTIR intensity change vs. dose curves were plotted only up to 425 MJ/m^2. This is because specimens exposed beyond this UV dose became very rough, which resulted in substantial increases in the standard deviations of both the bands of interest and the reference band, rendering the FTIR-ATR data unreliable. The intensity changes have been normalized to the least-changed band at 1380 cm^{-1} (i.e., adjusting so that the intensity of the 1380 cm^{-1} band (due to the gem-dimethyl group) is the same before and after exposure) to minimize the effect of surface morphological changes on the ATR probe-sample contact. It should be mentioned that, in the ATR technique, the intensity is a direct function of the contact area between the probe and the sample. However, the topography of a

polymer surface subjected to UV radiation tends to undergo inhomogeneous changes [47]. Therefore, the FTIR-ATR spectra taken from degraded samples must be normalized to an internal standard or to a least-changed band to compensate for surface morphological changes. The small error bars shown in Figure 3 indicate good reproducibility of the FTIR degradation data for both neat epoxy and MWCNT epoxy nanocomposite.

As seen in Figure 3, both neat epoxy and 3.5 % MWCNT epoxy nanocomposite samples underwent rapid chemical degradation under this UV/RH/T environment. The rates of intensity change with UV exposure between zero and 166 MJ/m^2 dose for the 1508 cm^{-1} (degradation) and 1726 cm^{-1} (oxidation) bands were similar for both materials. However, the degree of degradation and oxidation of the two materials differed thereafter. For the MWCNT epoxy nanocomposite, these changes reached a plateau at approximately 166 MJ/m^2 dose, but they continued to advance until 270 MJ/m^2 for the neat epoxy. A slight intensity decrease of the band at 1726 cm^{-1} at the highest dose, which is also seen in the spectra of Figure 2, is probably due to the substantial accumulation of MWCNTs on the sample surface (evidenced by SEM as presented in a later section). This would decrease the ATR probing depth in the oxidized epoxy layer. The higher resistance to degradation of the MWCNT epoxy nanocomposite than that of the neat epoxy observed in Figure 3 suggests that MWCNTs photostabilize the degradation of epoxy, similar to the results reported previously for 0.72 % MWCNT epoxy composite exposed to UV radiation [20] and for poly(methyl methacrylate) (PMMA) matrix containing various amounts of MWCNT subjected to high-energy radiation [48]. The photostabilization of polymers due to MWCNTs has been explained as due to the electron ring of the CNT network, which can disperse and filter the incident energy, and the strong interaction between free radicals (generated during irradiation) and CNTs [48]. The reversed trend of the spectrum at

425 MJ/m^2 observed in Figure 2B and 3B was probably due to both the rough surface topography caused by the photodegradation and the MWCNT layer accumulated on the surface (as shown later by SEM), which decreased the sample - ATR probe contact (hence intensity) and the band intensity of the epoxy matrix, respectively.

XPS spectra of the MWCNT epoxy nanocomposites at increasing doses of UV irradiation are presented in Figure 4A for the C (1s) region. Prior to UV irradiation (0 dose), the surface composition of the C (1s) region consisted of a broad, asymmetric peak located between 295 eV and 296 eV. This C (1s) feature is poorly resolved and shifted more than 10 eV towards higher binding energies, as compared to previous composite studies [7], due to the highly insulating nature of the epoxy. The epoxy control (Figure 4C, right) at 0 dose exhibited the same insulating properties, requiring the application of a charge neutralizer to properly resolve the spectra, whereas the MWCNT control (Figure 4C, left) was sufficiently conductive and did not require a charge neutralizer. When applying the neutralizer to the MWCNT epoxy nanocomposites (See Figure S5, 0 dose), a similar three component C (1s) region was observed that was comparable to the epoxy control. These observations of the pristine nanocomposites suggest that the initial surface was composed predominantly of epoxy.

As the UV dose increased up to 166 MJ/m^2, the most obvious change recorded by the XPS was a shift in the MWCNT nanocomposite's epoxy peak position from ≈ 295 eV to ≈ 289 eV (Figure 4A). This systematic shift of the C (1s) peak position towards binding energies typical of a carbon/nitrogen/oxygen containing polymer surface suggests that the surface of the MWCNT epoxy nanocomposite was becoming more conductive. Additionally, the C (1s) peak at low doses also appeared to gain some resolution, exhibited by a shoulder towards higher

binding energies. This may be a result of different chemical features, such as carbon bound to oxygen, becoming more evident due to reduced charging.

The presence of a new peak at ≈ 284.5 eV was the second change, as observed at a dose of 258 MJ/m^2 (Figure 4A). Interestingly, if one focuses in around 284.5 eV, the new contribution can be viewed at a dose as low as 92.3 MJ/m^2 and is definitely observed at 166 MJ/m^2 (See Figure 4B). This peak continued to grow to a dose of 775 MJ/m^2 at which point the spectrum was quite comparable with the MWCNT control samples (See Figure 4C, left), with the exception of a slightly more intense tail to higher binding energies. This suggests that the peak's presence is largely representative of the highly conductive MWCNT component dominating the surface of the UV exposed nanocomposite sample. The peak intensity at 284.5 eV subsided at 1090 MJ/m^2 and broadened, a phenomenon that may be attributed to either of the following: A) UV-induced damage to the surface of the CNT's as previously observed [49, 50]; or B) residual epoxy now re-exposed. Both of these choices would explain the observed transformation in the spectra but neither can be eliminated at this time. Lastly, the 'charged' epoxy peak that was around 289 eV drifted slowly to lower binding energies, becoming indistinguishable from the MWCNT tail and is perhaps the reason for a higher photoelectron count in the higher binding energy tail. Additionally, this may be the reason why the MWCNT peak changed slightly at 1090 MJ/m^2 where the oxidized epoxy contributions are sufficiently low enough to no longer charge and become part of the overall C (1s) spectra.

Qualitatively, Figure 4 demonstrates that the surface of the MWCNT epoxy nanocomposite is becoming dominated by the presence of MWCNTs with increasing UV dose in two ways. First, the most obvious change is of the development of the characteristic asymmetric peak representative of MWCNTs graphene-like carbon at 284.5 eV. Since XPS is surface

sensitive (depth of analysis < 10 nm) and the development of the MWCNT spectral feature is observed with and without the charge neutralizer at long UV exposures, this suggests that the surface concentration of MWCNTs was increasing. The benefit of *not* using the charge neutralizer is the ability to see the increase in the surface concentration of MWCNTs at much lower UV doses (Compare Figure 4 and Figure S5).

Secondly, the shift of the 'charged' epoxy peak to lower binding energies and subsequently diminishing in its presence suggests that the insulating properties of MWCNT epoxy nanocomposite are subsiding, likely due to the photo-oxidation of epoxy based material resulting in a corresponding increase in the surface concentration of MWCNTs. This photo-oxidative mechanism has been previously observed in other epoxy-based nanocomposites [7, 8]. Further evidence of an oxidation process can be observed in the charge neutralized XP spectra for the MWCNT epoxy nanocomposites at low doses (See Figure S5) and the UV exposed epoxy control (Figure 4C, right top) by the increase in highly oxidized C (denoted as COO prior). The photo-oxidative removal of the epoxy in the MWCNT epoxy nanocomposite samples is consistent with the decrease of the benzene ring absorbance at 1508 cm-1 and the increase in the aldehyde stretch at C=O as measured by ATR-FTIR (Figure 3) as well as the mass loss data (Figure 1).

3.3 *Effects of UV Irradiation on Nanocomposite Structure*

AFM images of the nanocomposites show that the exposure of MWCNTs on the nanocomposite surface increased with UV dose (Figure 5 A, B, and C). The exposed MWCNTs show up in these AFM images as nanometer-scale surface roughness, while the unexposed surface is comparatively smooth (Figure S6A). A higher resolution AFM image depicting how the individual MWCNTs contribute to the nanometer-scale surface roughness is shown in Figure

S7, while a comparison of the topography for neat epoxy and nanocomposite samples is shown in Figure S6. The surface of the 0 dose sample was nearly free of exposed MWCNTs (Figure S6A), while the surface of the highest UV exposed sample (1089 MJ/m^2) was almost completely covered by exposed MWCNTs (Figure 5C). The regions of exposed MWCNTs were topographically raised with respect to those areas that did not have exposed MWCNTs, with this height difference increased with UV dose. The initial surface started with sub-micron roughness (Figure S6A) and evolved to a micrometer-scale topography of "hills and valleys", where the highest and lowest features span a range of ≈ 8 μm (Figure 5C). We attribute the increasing height difference to screening of the epoxy degradation by the exposed MWCNTs. That is, once MWCNTs were exposed on the surface of the epoxy, those areas were at least partially protected from further epoxy degradation and surface mass loss. This is consistent with the results of Figures 1 and 3.

The surface morphology changes seen by AFM are also reflected in the SEM images (Figure 5D, 5E, and 5F). At a UV exposure of 166 MJ/m^2, the nanocomposite sample showed a relatively flat surface with pitting, undulation, and some areas of the subsurface MWCNT network beginning to become exposed (Fig. 5D). With increasing UV dose (425 MJ/m^2), surface roughness of the MWCNT nanocomposite increased and bundles of MWCNTs were clearly visible on the surface as shown in Figure 5E (top right corner), forming rough, uneven MWCNT hills and relatively smooth epoxy rich valleys. At 1089 MJ/m^2 of UV dose, the epoxy rich valleys became depleted leaving a surface of exposed undulating bundled MWCNTs (Figure 5F). The formation of an uneven distribution of MWCNT hills and valleys comes from the uneven sub-surface distribution of MWCNTs, as observed in charge contrast cross section SEM images (Figure S8) of the pristine nanocomposite.

Using EFTEM in the low-loss region on cross-sections, imaging can be performed where contrast between crystalline (i.e., MWCNTs) and amorphous (i.e., epoxy) carbonaceous phases can be distinguished [51]. The contrast can be further enhanced by two-window ratio imaging, where sample thickness artifacts can be normalized as long as the sample is not thick enough to have plural scattering [52]. The bright-field TEM images are shown in Figure S9 parts A, B, and C, while the EFTEM images used to obtain the EFTEM ratio images are shown in Figure S9 parts D through I. At a UV dose of 166 MJ/m^2, EFTEM of the cross sections showed MWCNTs near the surface, which is still relatively flat (Figure 5G), a result in agreement with the AFM and SEM images obtained for nancomposite samples irradiated with this UV dose (Figure 5 A and D). Upon further UV irradiation (425 MJ/m^2), EFTEM of the cross sections revealed a region of compressed MWCNTs at the surface (Figure 5H). After 1089 MJ/m^2 of UV exposure, EFTEM of the cross sections showed that the near-surface layer consisted primarily of a dense network of MWCNTs. Though the MWCNTs become highly exposed on the surface, the entanglement of MWCNTs in a network that has "roots" in the epoxy matrix may prevent the MWCNTs from readily being released from the surface.

3.4 *Potential for MWCNT Release Assessed Using Scratch Lithography*

In order to assess the attachment of the exposed nanotube layer to the bulk nanocomposite, we employed an AFM-based scratch test. Although the results of such a test are not directly comparable to tests performed using macroscopic abrasion tools, such as metal rakes or sanding wheels [17, 21, 53, 54], they can be used to assess whether the stress required to permanently deform the epoxy matrix is larger or smaller than the stress required to permanently deform the exposed nanotube layer. We expect that if the nanotube layer is more resistant to scratching than the matrix, then it is unlikely to be readily released from the surface.

AFM-based scratch lithography was used to assess the potential release of MWCNTs using the nanocomposite sample that had been exposed to a UV dose of 425 MJ/m^2. After the scratches were made on the surface, the surface damage was assessed using tapping mode AFM (Figure 6 A and B) and SEM (Figure 6 C and D). In Figure 6A, normal loads greater than 5 μN caused visible scratches in the MWCNT-covered region. In contrast, scratches were visible in the epoxy rich region (Figure 6 B) at loads as low as 0.5 μN. These results suggest that the region covered by MWCNTs was substantially more resistant to mechanical force compared to the epoxy region. However, the rough surface associated with the exposed MWCNTs region may have obscured small changes that would have been visible on the relatively smooth epoxy surface. In order to detect any such small changes to the MWCNT region, SEM was also performed on the post scratch lithography regions. At normal forces of 5 μN and 10 μN, the SEM images revealed multiple breaks in the MWCNTs in the scratch path (shown in Figure 6 C and D). In the zoomed-in region (Figure 6 D) of the 2.5 μN scratch path, no observable alteration in MWCNTs was evident. However, along the 1 μN path, discontinuities indicative of possible breaks in MWCNTs were detected. For normal loads smaller than 1 μN, no alterations in the MWCNTs along the scratch path were observed. While loads of 5 μN and 10 μN caused clear scratch lines in the MWCNT region based on the AFM data, SEM images showed relatively few break discontinuities in the MWCNTs. These loadings may have permanently compressed the MWCNTs into the surface, rather than breaking them or releasing them from the surface. In summary, both AFM and SEM measurements indicated that near the edge of the exposed MWCNT regions, the MWCNT covered regions were more mechanically resistant to scratching than the epoxy rich region.

The methods described in this manuscript can be used to assess different aspects of the transformations that can occur during UV irradiation of polymer CNT composites. Gravimetric measurements revealed changes to the bulk sample, while FTIR provided detailed chemical alterations of the polymer matrix. However, neither of these measurements provided information about the fate of MWCNTs. Conversely, microscopic (SEM, TEM, and AFM) and XPS measurements all revealed increasing MWCNT concentrations at the sample surface with higher UV doses. Importantly, XPS provided chemical confirmation on the presence of MWCNTs on the sample surface, while SEM and AFM analyses showed the presence of tube shaped structures that appeared to be MWCNTs but lacked definitive identification. The combination of XPS with SEM or AFM can provide identification of MWCNTs, their relative proximity, to the surface and information about the sample's surface topography. EFTEM analysis revealed that MWCNTs can be distinguished from the polymer background using the unique MWCNT chemical configuration, and confirmed the surface accumulation of MWCNTs. However, this technique requires significant user expertise and thus is unlikely to be used for routine analysis. Finally, scratch lithography has demonstrated the capability to assess the potential release of surface accumulated MWCNTs. Which set of techniques are most relevant for a particular investigation depends on what information is needed (potential for MWCNT release, information about the bulk sample, presence of MWCNTs on sample surface, etc.) and instrument availability.

4. Conclusions

By using a comprehensive suite of analytical methods we have identified two primary trends for MWCNT polymer composites exposed to UV radiation: a photostabilization effect from the presence of the MWCNT nanofiller and increasing accumulation of a dense, entangled

MWCNT layer on the surface of the nanocomposite samples with increasing UV dose. The increasing surface coverage by MWCNTs was strongly supported by both spectroscopic and microscopic techniques showing the convergence of the different methods. The results obtained by these methods show that the epoxy-rich surface layer of the nanocomposite is removed relatively rapidly, leaving a surface covered almost completely with MWCNTs.

The methods described in this manuscript, such as the innovative XPS method to identify MWCNTs on the surface of nanocomposite samples, are generally applicable for studies on related topics such as characterization of nanocomposites during manufacturing and assessment of MWCNT distribution in biological organisms. However, the scratch lithography results shown here and the lack of identifiable broken MWCNTs suggest that MWCNTs will not be readily released from the polymer nanocomposite, in agreement with most earlier studies [11-14, 16]. Additional research is needed to evaluate the conditions required (abrasion, hail, high wind, etc.) for MWCNT release from the MWCNT accumulated on the surface, to investigate the impact of UV irradiation using a broader range of conditions (i.e., different MWCNT loadings, polymers, MWCNT functionalization, and environmental stresses), and to assess the potential human health and ecological impacts of any released MWCNTs. Information on the formation and accumulation of a dense, entangled MWCNT layer on the nanocomposite surface after exposure to solar-like UV wavelengths is useful for assessing and mitigating the potential risks of MWCNT epoxy nanocomposites during their life cycles.

Acknowledgements

Disclaimer: Certain commercial product or equipment is described in this paper in order to specify adequately the experimental procedure. In no case does such identification imply

518 recommendation or endorsement by the National Institute of Standards and Technology, nor
519 does it imply that it is necessarily the best available for the purpose.

520 C. J. Long acknowledges support under the Cooperative Research Agreement between the
521 University of Maryland and the National Institute of Standards and Technology Center for
522 Nanoscale Science and Technology, Award 70NANB10H193, through the University of
523 Maryland.

524 **Supplementary Data**

525 Supporting information FTIR-ATR spectra, stack plot of XPS data from charge neutralized C
526 (1s) region, AFM image of unexposed MWCNT epoxy nanocomposite sample, SEM image of
527 freeze-fracture prepared cross-section of unexposed MWCNT epoxy nanocomposite sample, low
528 and high resolution AFM image comparisons, TEM and EFTEM images of MWCNT epoxy
529 nanocomposite samples after UR irradiation, SEM micrographs for size distribution of
530 MWCNTs used in the epoxy nanocomposites, figure describing preparation of epoxy
531 nanocomposite samples, and SEM images showing details for FIB sample preparation is
532 available in the online version of this article

533
534 **References**

535 [1] Baur, J.; Silverman, E., Challenges and opportunities in multifunctional nanocomposite
536 structures for aerospace applications. *MRS Bull.* **2007,** *32*, (4), 328-334.
537 [2] Lee, J.; Mahendra, S.; Alvarez, P. J. J., Nanomaterials in the construction industry: A review
538 of their applications and environmental health and safety considerations. *ACS Nano* **2010,** *4*, (7),
539 3580-3590.
540 [3] Nowack, B.; David, R. M.; Fissan, H.; Morris, H.; Shatkin, J. A.; Stintz, M., et al., Potential
541 release scenarios for carbon nanotubes used in composites. *Environ. Intl.* **2013,** *59*, (0), 1-11.
542 [4] Breuer, O.; Sundararaj, U., Big returns from small fibers: A review of polymer/carbon
543 nanotube composites. *Polym. Comp.* **2004,** *25*, (6), 630-645.
544 [5] Coleman, J. N.; Khan, U.; Blau, W. J.; Gun'ko, Y. K., Small but strong: A review of the
545 mechanical properties of carbon nanotube-polymer composites. *Carbon* **2006,** *44*, (9), 1624-
546 1652.

[6] Petersen, E. J.; Zhang, L. W.; Mattison, N. T.; O'Carroll, D. M.; Whelton, A. J.; Uddin, N., et al., Potential release pathways, environmental fate, and ecological risks of carbon nanotubes. *Environ. Sci. Technol.* **2011,** *45*, (23), 9837-9856.
[7] Gorham, J. M.; Nguyen, T.; Bernard, C.; Stanley, D.; Holbrook, R. D., Photo-induced surface transformations of silica nanocomposites. *Surf. Interface Anal.* **2012,** *44*, (13), 1572-1581.
[8] Nguyen, T.; Pellegrin, B.; Bernard, C.; Rabb, S.; Stuztman, P.; Gorham, J. M., et al., Characterization of Surface Accumulation and Release of Nanosilica During Irradiation of Polymer Nanocomposites by Ultraviolet Light. *J. Nanosci. Nanotechnol.* **2012,** *12*, (8), 6202-6215.
[9] Gottschalk, F.; Nowack, B., The release of engineered nanomaterials to the environment. *J. Environ. Monit.* **2011,** *13*, (5), 1145-1155.
[10] Asmatulu, R.; Mahmud, G. A.; Hille, C.; Misak, H. E., Effects of UV degradation on surface hydrophobicity, crack, and thickness of MWCNT-based nanocomposite coatings. *Progress in Organic Coatings* **2011,** *72*, (3), 553-561.
[11] Bello, D.; Wardle, B. L.; Yamamoto, N.; deVilloria, R. G.; Garcia, E. J.; Hart, A. J., et al., Exposure to nanoscale particles and fibers during machining of hybrid advanced composites containing carbon nanotubes. *J. Nano. Res.* **2009,** *11*, (1), 231-249.
[12] Bello, D.; Wardle, B. L.; Zhang, J.; Yamamoto, N.; Santeufemio, C.; Hallock, M., et al., Characterization of Exposures To Nanoscale Particles and Fibers During Solid Core Drilling of Hybrid Carbon Nanotube Advanced Composites. *Int. J. Occ. Saf. Environ. Health* **2010,** *16*, (4), 434-450.
[13] Cena, L. G.; Peters, T. M., Characterization and control of airborne particles emitted during production of epoxy/carbon nanotube nanocomposites. *J. Occ. Environ. Hyg.* **2011,** *8*, (2), 86-92.
[14] Wohlleben, W.; Brill, S.; Meier, M. W.; Mertler, M.; Cox, G.; Hirth, S., et al., On the Lifecycle of Nanocomposites: Comparing Released Fragments and their In-Vivo Hazards from Three Release Mechanisms and Four Nanocomposites. *Small* **2011,** *7*, (16), 2384-2395.
[15] Huang, G. N.; Park, J. H.; Cena, L. G.; Shelton, B. L.; Peters, T. M., Evaluation of airborne particle emissions from commercial products containing carbon nanotubes. *J. Nano. Res.* **2012,** *14*, (11).
[16] Wohlleben, W.; Meier, M. W.; Vogel, S.; Landsiedel, R.; Cox, G.; Hirth, S., et al., Elastic CNT–polyurethane nanocomposite: synthesis, performance and assessment of fragments released during use. *Nanoscale* **2013,** *5*, (1), 369-380.
[17] Schlagenhauf, L.; Chu, B. T. T.; Buha, J.; Nuesch, F.; Wang, J., Release of Carbon Nanotubes from an Epoxy-Based Nanocomposite during an Abrasion Process. *Environ. Sci. Technol.* **2012,** *46*, (13), 7366-7372.
[18] Armentano, I.; Dottori, M.; Puglia, D.; Kenny, J. M., Effects of carbon nanotubes (CNTs) on the processing and in-vitro degradation of poly(DL-lactide-co-glycolide)/CNT films. *J. Mater. Sci.: Mater. Med.* **2008,** *19*, (6), 2377-2387.
[19] van der Zande, M.; Sitharaman, B.; Walboomers, X. F.; Tran, L.; Ananta, J. S.; Veltien, A., et al., In vivo magnetic resonance imaging of the distribution pattern of gadonanotubes released from a degrading poly(lactic-co-glycolic acid) scaffold. *Tiss. Eng. C* **2011,** *17*, (1), 19-26.
[20] Nguyen, T.; Pelligrin, B.; Bernard, C.; Gu, X.; Gorham, J. M.; Stutzman, P., et al., Fate of nanoparticles during life cycle of polymer nanocomposites. *J. Phys. Conf. Ser.* **2011,** *304*, 012060.

[21] Hirth, S.; Cena, L.; Cox, G.; Tomović, Ž.; Peters, T.; Wohlleben, W., Scenarios and methods that induce protruding or released CNTs after degradation of nanocomposite materials. *J. Nano. Res.* **2013,** *15*, (4), 1-15.
[22] Petersen, E. J.; Henry, T. B., Methodological considerations for testing the ecotoxicity of carbon nanotubes and fullerenes: Review. *Environ. Toxicol. Chem.* **2012,** *31*, (1), 60-72.
[23] Aschberger, K.; Johnston, H. J.; Stone, V.; Aitken, R. J.; Hankin, S. M.; Peters, S. A. K., et al., Review of carbon nanotubes toxicity and exposure-Appraisal of human health risk assessment based on open literature. *Crit. Rev. Toxicol.* **2010,** *40*, (9), 759-790.
[24] National Institute for Occupational Safety and Health (NIOSH) *Current Intelligence Bulletin 65: Occupational Exposure to Carbon Nanotubes and Nanofibers*; 2013; p 156.
[25] Petersen, E. J.; Akkanen, J.; Kukkonen, J. V. K.; Weber, W. J., Jr., Biological uptake and depuration of carbon nanotubes by *Daphnia magna*. *Environ. Sci. Technol.* **2009,** *43*, (8), 2969-2975.
[26] Petersen, E. J.; Pinto, R. A.; Mai, D. J.; Landrum, P. F.; Weber, W. J., Jr., Influence of polyethyleneimine graftings of multi-walled carbon nanotubes on their accumulation and elimination by and toxicity to *Daphnia magna*. *Environ. Sci. Technol.* **2011,** *45*, (3), 1133-1138.
[27] Petersen, E. J.; Huang, Q. G.; Weber, W. J., Jr., Relevance of octanol-water distribution measurements to the potential ecological uptake of multi-walled carbon nanotubes. *Environ. Toxicol. Chem.* **2010,** *29*, (5), 1106-1112.
[28] Petersen, E. J.; Pinto, R. A.; Zhang, L.; Huang, Q. G.; Landrum, P. F.; Weber, W. J., Effects of polyethyleneimine-mediated functionalization of multi-walled carbon nanotubes on earthworm bioaccumulation and sorption by soils. *Environ. Sci. Technol.* **2011,** *45*, (8), 3718–3724.
[29] Ferguson, P. L.; Chandler, G. T.; Templeton, R. C.; Demarco, A.; Scrivens, W. A.; Englehart, B. A., Influence of sediment-amendment with single-walled carbon nanotubes and diesel soot on bioaccumulation of hydrophobic organic contaminants by benthic invertebrates. *Environ. Sci. Technol.* **2008,** *42*, (10), 3879-3885.
[30] Petersen, E. J.; Huang, Q. G.; Weber, W. J., Jr., Bioaccumulation of radio-labeled carbon nanotubes by *Eisenia foetida*. *Environ. Sci. Technol.* **2008,** *42*, (8), 3090-3095.
[31] Petersen, E. J.; Huang, Q. G.; Weber, W. J., Jr., Ecological uptake and depuration of carbon nanotubes by *Lumbriculus variegatus*. *Environ. Health Perspect.* **2008,** *116*, (4), 496-500.
[32] Petersen, E. J.; Nelson, B. C., Mechanisms and measurements of nanomaterial-induced oxidative damage to DNA. *Anal. Bioanal. Chem.* **2010,** *398*, 613-650.
[33] Kamal, M.; Huang, B., Natural and Artificial Weathering of Polymers. In *Handbook of Polymer Degradation*, Hamid, S.; Amin, M.; Maadhah, A., Eds. Marcel Dekker: New York, 1992; pp 127-178.
[34] Chin, J.; Byrd, E.; Embree, N.; Garver, J.; Dickens, B.; Finn, T., et al., Accelerated UV weathering device based on integrating sphere technology. *Rev. Sci. Instrum.* **2004,** *75*, (11), 4951-4959.
[35] O'Carroll, D. M.; Liu, X.; Mattison, N. T.; Petersen, E. J., Impact of diameter on carbon nanotube transport in sand. *J. Coll. Interf. Sci.* **2013,** *390*, 96-104.
[36] Robinson, J.; Linder, A.; Gemmel, A.; Poulsen, K. V.; Burkhard, H.; Högström, P., et al. In *Comparison of standard UV test methods for the ageing of cables*, 60th IWCS Conference, Charlotte, NC, 2011.
[37] Harrick, N. J., *Internal reflection spectroscopy*. 2nd ed.; Harrick Scientific Corporation: Ossining, NY, 1979.

[38] Nečas, D.; Klapetek, P., Gwyddion: an open-source software for SPM data analysis. *Central Eur. J. Phys.* **2012,** *10*, (1), 181-188.
[39] Loos, J.; Alexeev, A.; Grossiord, N.; Koning, C. E.; Regev, O., Visualization of single-wall carbon nanotube (SWNT) networks in conductive polystyrene nanocomposites by charge contrast imaging. *Ultramicroscopy* **2005,** *104*, (2), 160-167.
[40] Mayer, J.; Giannuzzi, L. A.; Kamino, T.; Michael, J., TEM sample preparation and FIB-induced damage. *MRS Bull.* **2007,** *32*, (5), 400-407.
[41] Schaffer, B.; Grogger, W.; Kothleitner, G., Automated spatial drift correction for EFTEM image series. *Ultramicroscopy* **2004,** *102*, (1), 27-36.
[42] Walters, D. A.; Cleveland, J. P.; Thomson, N. H.; Hansma, P. K.; Wendman, M. A.; Gurley, G., et al., Short cantilevers for atomic force microscopy. *Rev. Sci. Instrum.* **1996,** *67*, (10), 3583-3590.
[43] Rabek, J. F., *Polymer Photodegradation: Mechanism and Experimental Methods*, Chapman & Hall: NY, 1995; pp 185-216.
[44] Bellenger, V.; Verdu, J., Oxidative skeleton breaking in epoxy-amine networks. *J. Appl. Polym. Sci.* **1985,** *30*, (1), 363-374.
[45] Rivaton, A.; Moreau, L.; Gardette, J. L., Photo-oxidation of phenoxy resins at long and short wavelengths - II. Mechanisms of formation of photoproducts. *Polym. Degrad. Stab.* **1997,** *58*, (3), 333-339.
[46] Mailhot, N.; Morlat-Theias, S.; Ouahioune, M.; Gardette, J. L., Study of the degradation of an epoxy/amine resin, 1 photo- and thermo-chemical mechanisms. *Macromol. Chem. Phys.* **2005,** *206*, (5), 575-584.
[47] Nguyen, T.; Gu, X.; Vanlandingham, M.; Byrd, E.; Ryntz, R.; Martin, J. W., Degradation modes of crosslinked coatings exposed to photolytic environment. *J. Coat. Technol. Res.* **2013,** *10*, (1), 1-14.
[48] Najafi, E.; Shin, K., Radiation resistant polymer-carbon nanotube nanocomposite thin films. *Colloids Surf., A* **2005,** *257-58*, 333-337.
[49] Parekh, B.; Debies, T.; Knight, P.; Santhanam, K. S. V.; Takacs, G. A., Surface functionalization of multiwalled carbon nanotubes with UV and vacuum UV photo-oxidation. *J. Adhes. Sci. Technol.* **2006,** *20*, (16), 1833-1846.
[50] Simmons, J. M.; Nichols, B. M.; Baker, S. E.; Marcus, M. S.; Castellini, O. M.; Lee, C. S., et al., Effect of ozone oxidation on single-walled carbon nanotubes. *J. Phys. Chem. B* **2006,** *110*, (14), 7113-7118.
[51] Daniels, H. R.; Brydson, R.; Brown, A.; Rand, B., Quantitative valence plasmon mapping in the TEM: viewing physical properties at the nanoscale. *Ultramicroscopy* **2003,** *96*, (3-4), 547-558.
[52] Gass, M. H.; Koziol, K. K. K.; Windle, A. H.; Midgley, P. A., Four-dimensional spectral tomography of carbonaceous nanocomposites. *Nano Lett.* **2006,** *6*, (3), 376-379.
[53] Kuhlbusch, T. A.; Asbach, C.; Fissan, H.; Gohler, D.; Stintz, M., Nanoparticle exposure at nanotechnology workplaces: a review. *Part. Fibre Toxicol.* **2011,** *8*, 22.
[54] Golanski, L.; Guiot, A.; Pras, M.; Malarde, M.; Tardif, F., Release-ability of nano fillers from different nanomaterials (toward the acceptability of nanoproduct). *J. Nano. Res.* **2012,** *14*, (7).

683

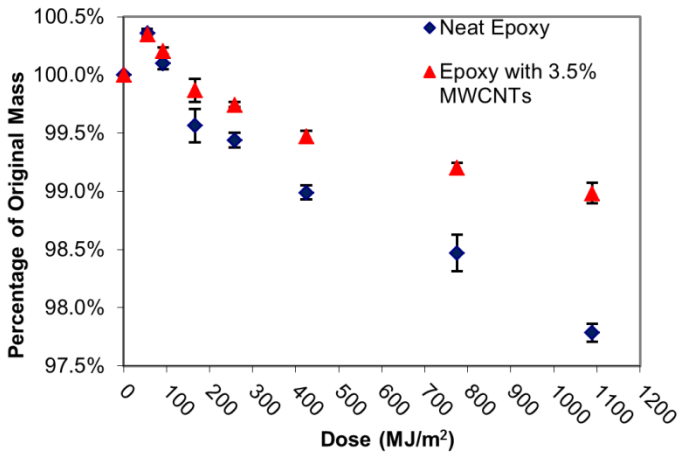

684

685 **Figure 1.** Mass loss as a function of UV radiation dose for neat epoxy and 3.5% MWCNT epoxy
686 nanocomposite samples exposed to UV at 50 ºC and 75% relative humidity. Results are the
687 average of five specimens, and error bars represent one standard deviation.

688

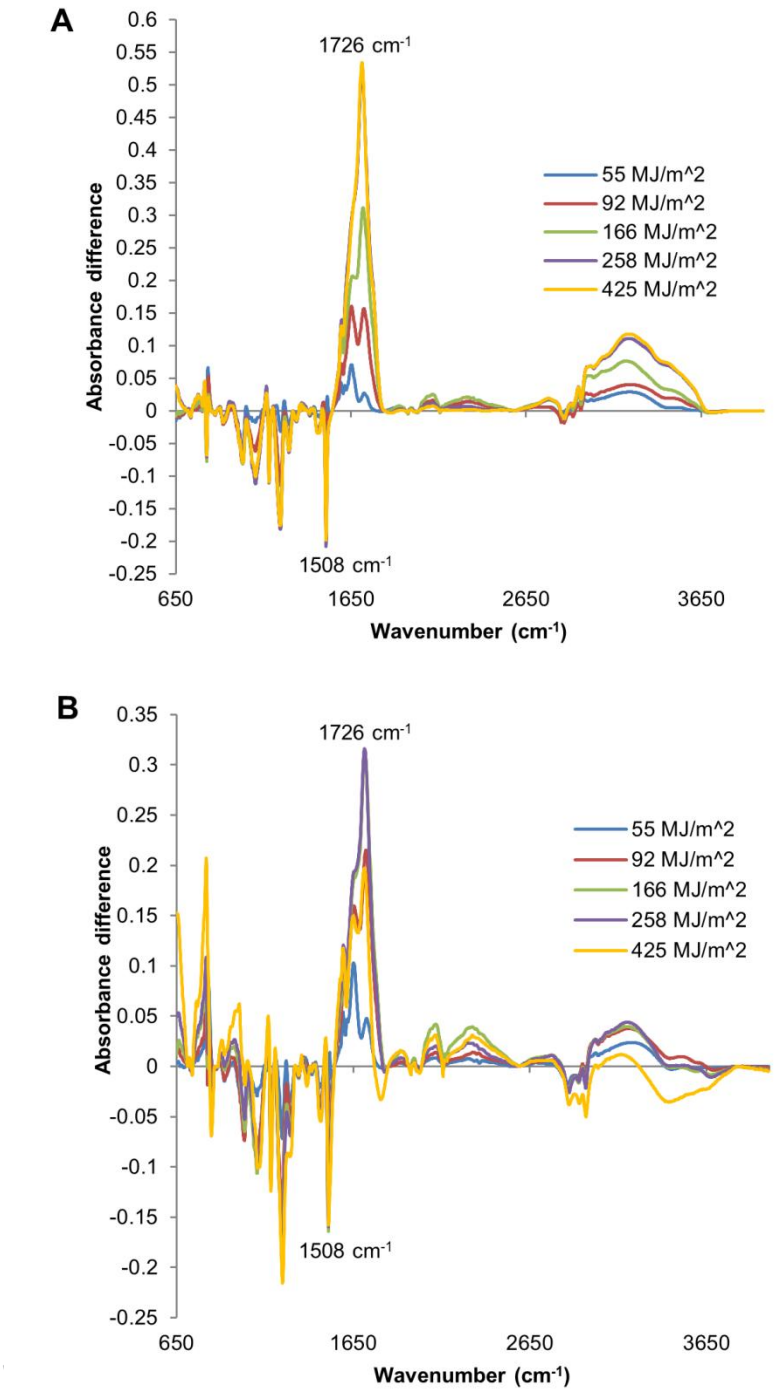

689

690 **Figure 2.** Difference FTIR-ATR spectra recorded at different UV irradiation doses for (A) neat

691 epoxy, and (B) 3.5 % MWCNT epoxy nanocomposite.

692

693

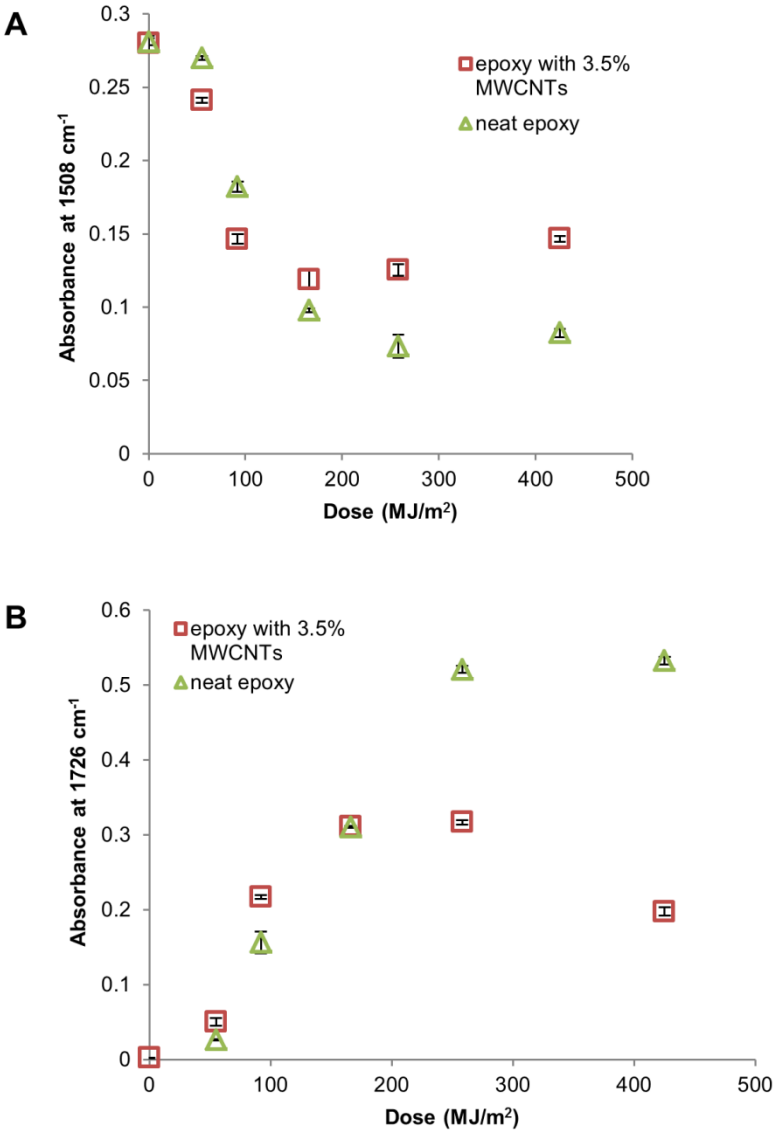

694

695 **Figure 3.** Changes in FTIR-ATR intensity for (A) 1508 cm^{-1} and (B) 1726 cm^{-1} bands for neat
696 epoxy and 3.5% MWCNT epoxy nanocomposite samples before and after UV irradiation with
697 varying doses. Each data point was the average of three specimens, and the error bars represent
698 one standard deviation.

699

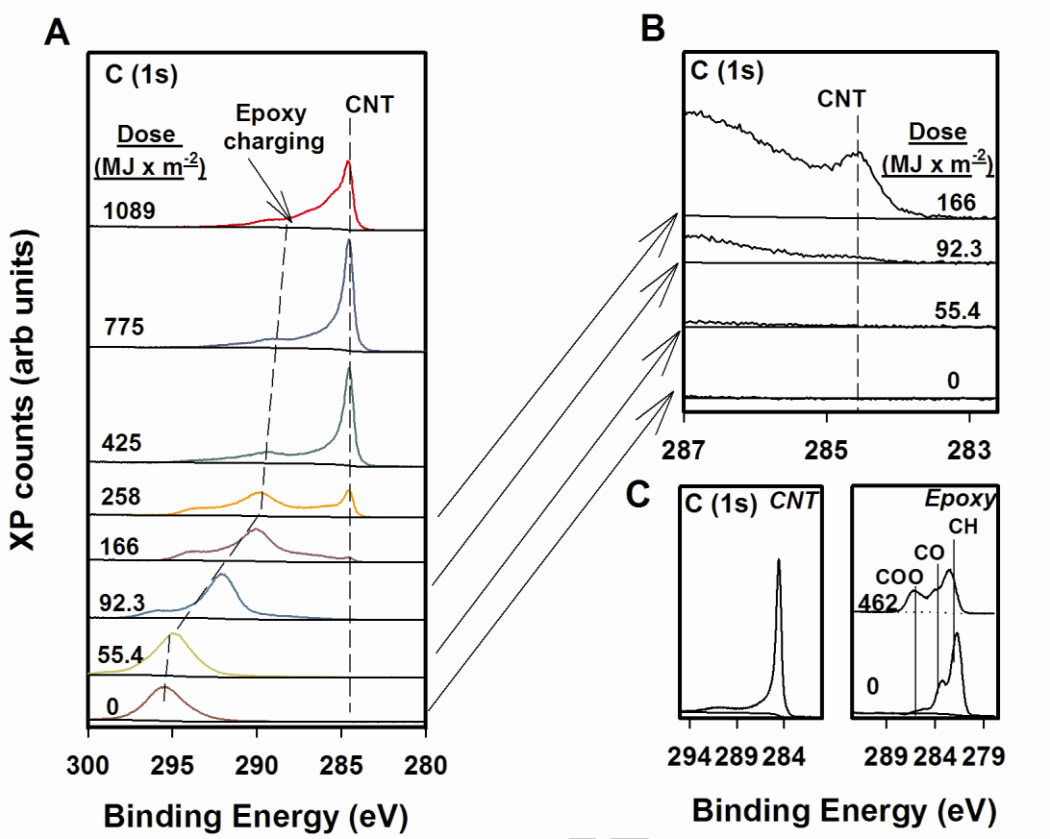

700

701 **Figure 4.** XPS results of the surface transformations of MWCNT epoxy nanocomposites with

702 increasing dose of UV irradiation. A) Stack plot of the C (1s) region from 0 to 1089 MJ/m^2. B)

703 Magnification of low dose studies with a focus on the CNT component of the C (1s) region. C)

704 Control spectra of pure CNT powder (left) and epoxy (right). The pure epoxy sample has a

705 reference at 0 and 462 MJ/m^2 UV dose.

706

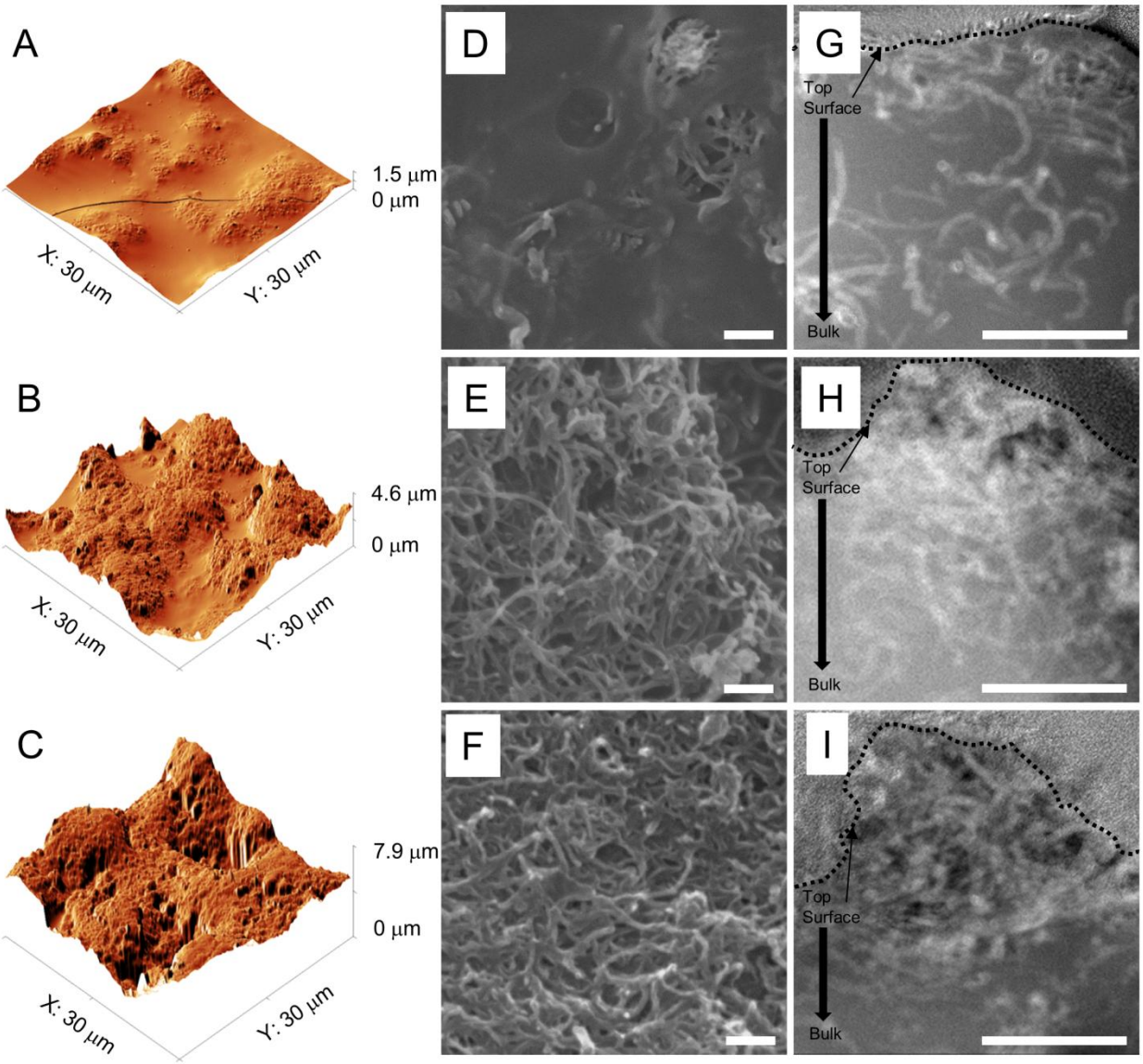

Figure 5. Microscopic evaluation of MWCNT epoxy nanocomposite samples using AFM (A, B, C), SEM (D, E, F), and EFTEM (G, H, I). The samples were exposed to UV doses of 166 MJ/m^2 (A, D, G), 425 MJ/m^2 (B, E, H), and 1089 MJ/m^2 (C, F, I). 3D AFM images and SEM images are of the surface while EFTEM images are of cross-sections prepared by a focused ion beam. The boundary of the top surface of the nanocomposite is highlighted by the dash line. Scale bars for SEM and EFTEM images are 200 nm.

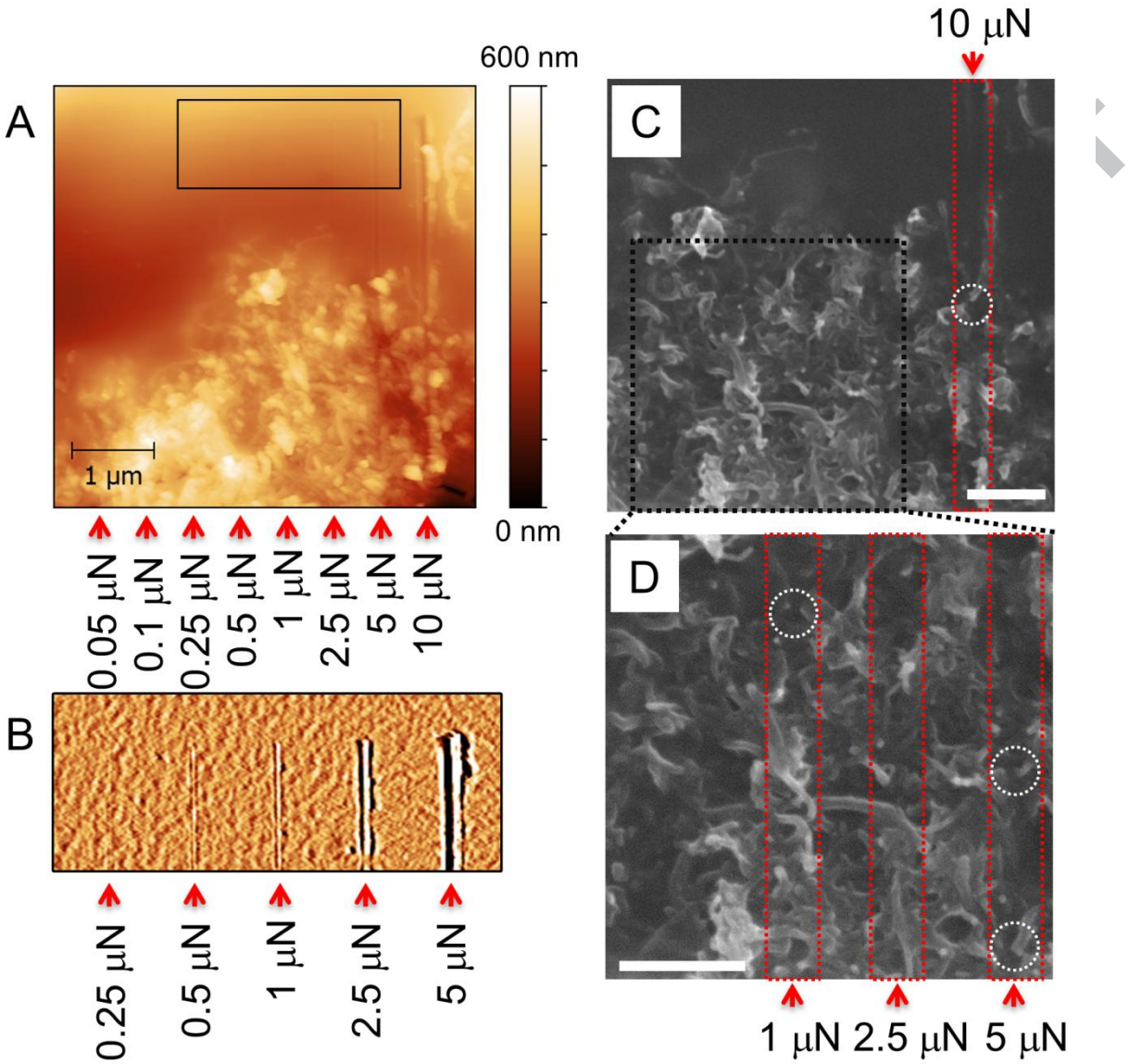

Figure 6. AFM scratch lithography on the MWCNT epoxy nanocomposite sample exposed to 425 MJ/m^2 UV dose. The normal force at each scratch path is indicated by arrows. (A) AFM topography image after scratching and (B) filtered AFM topography image of the boxed region shown in part A. (C, D) Post scratch lithography examination in SEM. SEM scale bars are 500nm. Specific breaks in MWCNTs are highlighted by circles.